Acta Mechanica Solida Sinica
https://doi.org/10.1007/s10338-026-00800-2

Finite Electromechanical Response of Fiber-Reinforced Dielectric Elastomer Tubes Under Combined Loadings

Renwei Mao[1,2] · Congshan Liu[3] · Guozhan Xia[4] · Weiqiu Chen[1,2] · Michel Destrade[2,5] · Yipin Su[1,2,6]

Received: 19 February 2026 / Revised: 12 June 2026 / Accepted: 14 June 2026

Abstract

Fiber-reinforced dielectric elastomers have emerged as promising materials for soft actuators due to their enhanced mechanical stability and tunable electromechanical properties. This paper presents a comprehensive theoretical framework for analyzing the finite electromechanical response of thick-walled cylindrical dielectric elastomer tubes with axial fiber reinforcement subjected to combined radial voltage, internal pressure, and axial loading. Based on the nonlinear electroelastic theory for transversely isotropic materials, we derive analytical solutions for the deformation, stress distribution, and electric field under either axially constrained or axially free boundary condition. The formulation introduces fiber-induced anisotropic invariants into the electroelastic energy function and accommodates arbitrary material models. We find that axial pre-stretch significantly enhances voltage-driven actuation while reducing the risk of electrical breakdown, and fiber reinforcement suppresses electromechanical instabilities and stabilizes the nonmonotonic force–deformation response under combined loading. Moreover, the material's strain-limiting behavior plays a critical role in preventing catastrophic thinning and electrical failure. The results provide new physical insights into the role of fiber reinforcement in regulating electromechanical coupling and offer quantitative design guidelines for stable and efficient dielectric elastomer tubular actuators in applications such as soft robotics, artificial muscles, and adaptive structures.

Keywords Dielectric elastomer · Fiber reinforcement · Electroelasticity · Finite deformation

1 Introduction

Dielectric elastomers (DEs) constitute an important class of soft electroactive materials capable of converting electrical stimuli into large and reversible mechanical deformations. Their high compliance, large actuation strain exceeding 100%, fast response, and high energy density have motivated extensive research on dielectric elastomer actuators (DEAs) for applications in soft robotics, artificial muscles, adaptive structures, and bio-inspired devices [1–8]. Among various DEA configurations, cylindrical dielectric tubes are particularly attractive. With compliant electrodes on the inner and outer surfaces, a radial electric field is naturally established, producing Maxwell stresses across the thickness. This configuration enables efficient electromechanical coupling and allows the axial response to be tailored through prescribed axial stretch or force. Compared with planar membranes, dielectric tubes exhibit superior load-bearing capacity, geometric robustness, and intrinsic compatibility with pressurized environments, making them well suited for fluid-driven or electro-pneumatic actuation [9–12].

✉ Guozhan Xia
guozhan.xia@unitn.it

✉ Yipin Su
su_yp@zju.edu.cn

1 Huanjiang Laboratory, Zhejiang University, Zhuji 311800, China

2 Department of Engineering Mechanics, Zhejiang University, Hangzhou 310027, China

3 Center for Mechanics Plus Under Extreme Environments, Ningbo University, Ningbo 315211, China

4 Department of Civil, Environmental and Mechanical Engineering, University of Trento, 38123 Trento, Italy

5 School of Mathematical and Statistical Sciences, University of Galway, Galway, Ireland

6 School of Civil Engineering, Shaoxing University, Shaoxing 312000, China

Published online: 09 July 2026

The theoretical description of deformation of DEs is framed within nonlinear theory of electroelasticity. Dorfmann and Ogden [13] proposed a comprehensive framework for nonlinear electroelasticity based on invariant decompositions, which has become the standard foundation for analyzing DE structures. These frameworks have been widely applied to investigate deformation, bifurcation, and failure of DE structures [14–18]. Suo and colleagues developed stability criteria for dielectric elastomers under various electromechanical loading conditions [19, 20].

Despite these advances, conventional dielectric elastomers are nearly isotropic and mechanically soft, making DEs prone to instability and limiting their load-carrying capability. Introducing anisotropy via fiber reinforcement provides an effective route to overcome these limitations. The incorporation of fibers fundamentally alters the material's mechanical response and significantly improves dimensional stability, load-bearing capacity, and resistance to electromechanical instability [21]. Xiao et al. [22] demonstrated that fiber reinforcement can suppress electromechanical instability by introducing strain-stiffening effects that counteract voltage-induced softening, thereby expanding the stable actuation regime.

For fiber-reinforced dielectric elastomers, the constitutive framework must account for both the material anisotropy introduced by fiber alignment and the electromechanical coupling. Bustamante [23] developed a comprehensive constitutive framework for transversely isotropic nonlinear electroactive elastomers, establishing the theoretical foundation widely adapted for modeling fiber-reinforced dielectric systems. His work extended nonlinear electroelasticity theory to account for material anisotropy through additional invariants associated with the fiber direction. In recent years, considerable efforts have also been devoted to understanding the electromechanical behavior of fiber-reinforced dielectric elastomer cylindrical actuators. For example, Goulbourne et al. [24] developed a mathematical model for cylindrical dielectric elastomer actuators, demonstrating how cylindrical geometry and constraints fundamentally alter deformation modes and force output under combined pressure and electrical loading. He et al. [25] investigated the voltage-induced torsional deformation of a dielectric elastomer tube reinforced by helical fibers. They revealed that snap-through instability causes the twist angle to jump from the unbulged state to the bulged state. Liu and Yong [26] developed a theoretical model for finite-thickness fiber-reinforced dielectric elastic tubular actuators under combined electromechanical loadings. They characterized the dependence of critical and Maxwell stretches on fiber parameters during bulge evolution. Their study demonstrated that helical fibers with high angles and stiffnesses can change the instability characteristics from limit-point instability to snap-through instability.

Although existing studies have demonstrated the potential of reinforcement and constraints in dielectric cylindrical actuators, critical limitations remain. Much of the literature focuses on specific actuation modes or adopts idealized assumptions such as membrane behavior. Investigations of thick-walled fiber-reinforced dielectric tubes subjected simultaneously to radial voltage, internal pressure, and axial force have not been systematically elucidated within a unified theoretical framework. The present study aims to fill this gap by developing a nonlinear electromechanical model for a finite-thickness, axially fiber-reinforced dielectric tube and by investigating its coupled deformation behavior under multiple concurrent loadings.

The paper is structured as follows. Section 2 presents the theoretical framework of nonlinear electroelasticity for fiber-reinforced dielectric elastomers, including kinematics, field measures, and the constitutive formulation with anisotropic invariants. In Sect. 3, we formulate the boundary value problem for a thick-walled cylindrical tube with axial fiber reinforcement subjected to radial voltage, internal pressure, and axial loading, and derive the governing equations for both axially constrained and axially free conditions. Section 4 specializes the general theory to specific material models and clarifies the loading conditions of the structure. Numerical results are presented in Sect. 5, where we systematically investigate the effects of fiber reinforcement, pre-stretch, voltage, and material parameters on the electromechanical response. Finally, Sect. 6 summarizes the main findings and discusses their implications for the design of fiber-reinforced dielectric elastomer actuators.

2 Nonlinear Electroelasticity for Fiber-Reinforced Dielectric Elastomers

This section presents a brief overview of the nonlinear electroelasticity theory for fiber-reinforced dielectric elastomers. For comprehensive treatments, the reader is referred to [13, 23].

2.1 Kinematics and Field Measures

Consider a deformable electrostatic body which occupies an undeformed, stress-free reference configuration $\mathcal{B}_0$ with boundary $\partial\mathcal{B}_0$ and outward unit normal $\mathbf{N}$. A material point is labeled by its position vector $\mathbf{X} \in \mathcal{B}_0$. After a finite motion, the body occupies the current configuration $\mathcal{B}$ with boundary $\partial\mathcal{B}$ and outward unit normal $\mathbf{n}$, and the motion is described by the mapping

$$\mathbf{x} = \boldsymbol{\chi}(\mathbf{X}, t). \tag{1}$$

The deformation gradient is

$$\mathbf{F} = \frac{\partial \mathbf{x}}{\partial \mathbf{X}}, \tag{2}$$

with the right and left Cauchy–Green tensors defined by

$$\mathbf{C} = \mathbf{F}^{\mathrm{T}}\mathbf{F}, \qquad \mathbf{b} = \mathbf{F}\mathbf{F}^{\mathrm{T}}, \tag{3}$$

respectively.

We focus on incompressible elastomers, so

$$J = \det \mathbf{F} \equiv 1. \tag{4}$$

Let $\mathbf{E}$ and $\mathbf{D}$ denote the true (Eulerian) electric field and electric displacement in $\mathcal{B}$. Their Lagrangian counterparts are introduced as

$$\mathbf{E}_L = \mathbf{F}^{\mathrm{T}}\mathbf{E}, \qquad \mathbf{D}_L = \mathbf{F}^{-1}\mathbf{D}. \tag{5}$$

2.2 Governing Equations and Boundary Conditions

Under the quasi-electrostatic approximation and in the absence of free volume charges and currents, the field equations in the current configuration $\mathcal{B}$ read

$$\mathrm{curl}\mathbf{E} = \mathbf{0}, \qquad \mathrm{div}\mathbf{D} = \mathbf{0}. \tag{6}$$

Mechanical equilibrium (no body forces) is written in terms of the total Cauchy stress $\boldsymbol{\tau}$ as

$$\mathrm{div}\boldsymbol{\tau} = \mathbf{0}. \tag{7}$$

Across the boundary $\partial\mathcal{B}$, the electrostatic continuity conditions are

$$\mathbf{n} \times [\![\mathbf{E}]\!] = \mathbf{0}, \qquad \mathbf{n} \cdot [\![\mathbf{D}]\!] = 0, \tag{8}$$

where $[\![\cdot]\!]$ denote the electric field and electric displacement in the surrounding vacuum, respectively. These conditions ensure continuity of the tangential electric field and normal electric displacement. The mechanical traction condition is

$$\boldsymbol{\tau}\mathbf{n} = \mathbf{t}_a + \mathbf{t}_M^{\mathrm{out}} \quad \text{on } \partial\mathcal{B}_t, \tag{9}$$

where $\mathbf{t}_a$ is the prescribed mechanical traction and $\mathbf{t}_M^{\mathrm{out}} = \boldsymbol{\tau}_M^{\mathrm{out}}\mathbf{n}$ is the traction associated with the Maxwell stress in the exterior medium. In vacuum, the Maxwell stress is

$$\boldsymbol{\tau}_M^{\mathrm{out}} = \varepsilon_0 \left[\mathbf{E}^{\mathrm{out}} \otimes \mathbf{E}^{\mathrm{out}} - \frac{1}{2}\left(\mathbf{E}^{\mathrm{out}} \cdot \mathbf{E}^{\mathrm{out}}\right)\mathbf{I}\right], \tag{10}$$

where $\mathbf{E}^{\mathrm{out}}$ denotes the electric field in the surrounding vacuum, ε_0 is the vacuum permittivity, and $\mathbf{I}$ is the second-order identity tensor.

2.3 Constitutive Framework for Transversely Isotropic Dielectric Elastomers

We consider a transversely isotropic electroelastic solid reinforced by a single family of fibers. Let $\mathbf{M}$ be the unit fiber direction in the reference configuration $\mathcal{B}_0$. Its current (push-forward) direction is along $\mathbf{m} = \mathbf{F}\mathbf{M}$.

We assume the existence of an augmented free-energy density (per unit reference volume)

$$\Omega = \Omega\left(\mathbf{F}, \mathbf{E}_L, \mathbf{M}\right), \tag{11}$$

and, for incompressibility, the work-conjugate constitutive relations are

$$\mathbf{T} = \mathbf{F}^{-1}\boldsymbol{\tau} = \frac{\partial \Omega}{\partial \mathbf{F}} - p\mathbf{F}^{-1}, \qquad \mathbf{D}_L = \mathbf{F}^{-1}\mathbf{D} = -\frac{\partial \Omega}{\partial \mathbf{E}_L}, \tag{12}$$

where p is the Lagrange multiplier enforcing $J = 1$, and $\mathbf{T}$ is the nominal stress.

By material objectivity, Ω depends on $\mathbf{F}$ through $\mathbf{C}$, and a convenient invariant set is

$$\begin{gathered} I_1 = \mathrm{tr}\mathbf{C}, \quad I_2 = \mathrm{tr}\mathbf{C}^{-1}, \quad I_4 = \mathbf{E}_L \cdot \mathbf{E}_L, \quad I_5 = \mathbf{E}_L \cdot \mathbf{C}^{-1}\mathbf{E}_L, \quad I_6 = \mathbf{E}_L \cdot \mathbf{C}^{-2}\mathbf{E}_L, \\ I_7 = \mathbf{M} \cdot \mathbf{C}\mathbf{M}, \quad I_8 = \mathbf{M} \cdot \mathbf{C}^2\mathbf{M}, \quad I_9 = \mathbf{M} \cdot \mathbf{E}_L, \quad I_{10} = \mathbf{M} \cdot \mathbf{C}\mathbf{E}_L, \end{gathered} \tag{13}$$

where I_1 and I_2 are the standard isotropic strain invariants, I_4-I_6 capture electromechanical coupling, and I_7-I_{10} account for the fiber-induced anisotropy.

For incompressible materials, the total Cauchy stress $\boldsymbol{\tau}$ and the true electric displacement $\mathbf{D}$ can be written explicitly in terms of $\mathbf{b}$, $\mathbf{E}$, and the current fiber vector $\mathbf{m}$, by combining Eqs. (12) and (13) as

$$\begin{aligned} \boldsymbol{\tau} = {} & 2\Omega_1\mathbf{b} + 2\Omega_2\left(I_1\mathbf{b} - \mathbf{b}^2\right) - p\mathbf{I} - 2\Omega_5\mathbf{E} \otimes \mathbf{E} - 2\Omega_6\left(\mathbf{b}^{-1}\mathbf{E} \otimes \mathbf{E} + \mathbf{E} \otimes \mathbf{b}^{-1}\mathbf{E}\right) \\ & + 2\Omega_7\mathbf{m} \otimes \mathbf{m} + 2\Omega_8(\mathbf{m} \otimes \mathbf{bm} + \mathbf{bm} \otimes \mathbf{m}) + \Omega_{10}(\mathbf{m} \otimes \mathbf{bE} + \mathbf{bE} \otimes \mathbf{m}), \end{aligned} \tag{14}$$

$$\mathbf{D} = -2\left(\Omega_4\mathbf{bE} + \Omega_5\mathbf{E} + \Omega_6\mathbf{b}^{-1}\mathbf{E}\right) - \Omega_9\mathbf{m} - \Omega_{10}\mathbf{bm}, \tag{15}$$

where $\Omega_i = \partial\Omega/\partial I_i$ for $i = 1, 2, ..., 10$. These constitutive equations generalize the isotropic electroelastic relations to account for fiber-induced anisotropy, with the terms involving Ω_7-Ω_{10} representing the additional contributions from fiber deformation and fiber-field coupling.

3 Finite Inflation of Fiber-Reinforced Dielectric Tubes

3.1 Geometry, Deformation Kinematics, and Field Distributions

Consider a cylindrical tube made of fiber-reinforced dielectric elastomer, with fibers aligned along the axial direction characterized by $\mathbf{M} = \begin{pmatrix} 0 & 0 & 1 \end{pmatrix}^{\mathrm{T}}$ in the reference configuration, as shown in Fig. 1. The tube has inner radius R_{i} and outer radius R_{o}, with the thickness ratio defined as $t = R_{\mathrm{i}}/R_{\mathrm{o}} \in (0, 1)$. Compliant electrodes are bonded to the inner and outer cylindrical surfaces to apply a radial voltage V, while an internal pressure P acts on the inner surface.

The undeformed configuration $\mathcal{B}_0$ is described in cylindrical coordinates (R, Θ, Z) as

$$R_{\mathrm{i}} \le R \le R_{\mathrm{o}}, \quad 0 \le \Theta \le 2\pi, \quad 0 \le Z \le L, \tag{16}$$

where L denotes the initial tube length. Under the combined electromechanical loading, the tube undergoes radially inhomogeneous inflation accompanied by axial stretch. The deformation is described by

$$R^2 - R_{\mathrm{i}}^2 = \lambda_z (r^2 - r_{\mathrm{i}}^2), \quad \theta = \Theta, \quad z = \lambda_z Z, \tag{17}$$

where (r, θ, z) denote the current cylindrical coordinates, λ_z is the uniform axial stretch, and r_{i} and r_{o} are the deformed inner and outer radii, respectively. From Eq. (2), the deformation gradient tensor takes the diagonal form

$$\mathbf{F} = \mathrm{diag}\left(\frac{1}{\lambda\lambda_z},\ \lambda,\ \lambda_z\right), \tag{18}$$

where the circumferential principal stretch is

$$\lambda = \frac{r}{R}. \tag{19}$$

At the inner and outer surfaces, we denote $\lambda_{\mathrm{i}} = r_{\mathrm{i}}/R_{\mathrm{i}}$ and $\lambda_{\mathrm{o}} = r_{\mathrm{o}}/R_{\mathrm{o}}$, respectively.

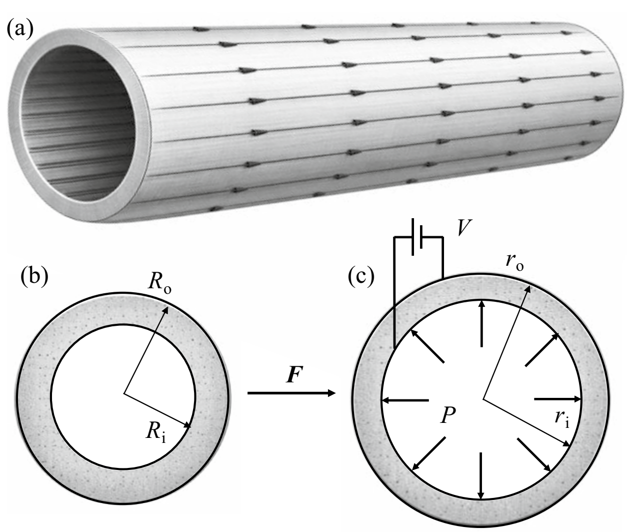

Fig. 1 Schematic illustration of the deformation of a fiber-reinforced dielectric cylindrical tube: **a** Three-dimensional view of the tube in the undeformed configuration, in which reinforcing fibers are aligned along the axial (lengthwise) direction of the tube; **b** Cross-sectional view of the tube in the undeformed configuration, characterized by the inner radius R_{i} and outer radius R_{o}; **c** Cross-sectional view of the tube in the deformed configuration, subjected to an internal pressure P and a radial electric field generated by compliant electrodes applied on the inner and outer surfaces, leading to the deformed inner and outer radii r_{i} and r_{o}, respectively

From Eqs. (17) and (19), the radial coordinate r can be expressed as

$$r = \lambda \sqrt{\frac{\lambda_z r_{\mathrm{i}}^2 - R_{\mathrm{i}}^2}{\lambda^2 \lambda_z - 1}}, \tag{20}$$

and the outer circumferential stretch λ_{o} is related to λ_{i} and λ_z through the incompressibility constraint:

$$\lambda_{\mathrm{o}} = \sqrt{\frac{1 - t^2 + \lambda_z \lambda_{\mathrm{i}}^2 t^2}{\lambda_z}}. \tag{21}$$

A crucial differential relation, obtained by differentiating Eq. (20), is

$$\frac{\mathrm{d}r}{\mathrm{d}\lambda} = \frac{r}{\lambda(1 - \lambda_z \lambda^2)}, \tag{22}$$

which will be instrumental in transforming spatial integrals into stretch-domain integrals.

In the Lagrangian description, the nominal and true electric fields are purely radial: $\mathbf{E}_L = \begin{pmatrix} E_{LR} & 0 & 0 \end{pmatrix}^{\mathrm{T}}$ and $\mathbf{E} = \begin{pmatrix} E_r & 0 & 0 \end{pmatrix}^{\mathrm{T}}$, with $E_r = \lambda\lambda_z E_{LR}$. For our problem, Eq. $(6)_1$ is automatically satisfied. The radial electric field is established by applying voltage across compliant electrodes bonded to the inner and outer cylindrical surfaces, which eliminates the electric field in the surrounding medium [27].

Using the deformation gradient (18), the nonzero invariants defined in Eq. (13) are evaluated as

$$\begin{aligned} I_1 &= \lambda^2 + \frac{1}{\lambda^2\lambda_z^2} + \lambda_z^2, \quad I_2 = \frac{1}{\lambda^2} + \frac{1}{\lambda_z^2} + \lambda^2\lambda_z^2, \quad I_4 = E_{LR}^2, \\ I_5 &= \lambda^2\lambda_z^2 E_{LR}^2, \quad I_6 = \lambda^4\lambda_z^4 E_{LR}^2, \quad I_7 = \lambda_z^2, \quad I_8 = \lambda_z^4. \end{aligned} \tag{23}$$

Substituting these invariants into the general stress relation (14), the nonzero Cauchy stress components in cylindrical coordinates are

$$\begin{aligned} \tau_{rr} &= \frac{2}{\lambda^2\lambda_z^2}\left[\Omega_1 + (\lambda^2 + \lambda_z^2)\Omega_2 - \lambda^4\lambda_z^2 E_{LR}^2 \Omega_5 - 2\lambda^6\lambda_z^6 E_{LR}^2 \Omega_6\right] - p, \\ \tau_{\theta\theta} &= 2\lambda^2\Omega_1 + 2\left(\frac{1}{\lambda_z^2} + \lambda^2\lambda_z^2\right)\Omega_2 - p, \\ \tau_{zz} &= 2\lambda_z^2\Omega_1 + \left(\frac{2}{\lambda^2} + 2\lambda^2\lambda_z^2\right)\Omega_2 + 2\lambda_z^2\Omega_7 + 4\lambda_z^4\Omega_8 - p, \\ \tau_{rz} &= \frac{E_{LR}\Omega_{10}}{\lambda}. \end{aligned} \tag{24}$$

It is noteworthy that a nonzero shear stress component τ_{rz} emerges due to the coupling between the fiber orientation, mechanical deformation, and the radial electric field through the invariant $I_{10} = \mathbf{M} \cdot \mathbf{C}\mathbf{E}_L$.

From Eq. (15), the electric displacement components are

$$
\begin{aligned}
D_r &= -\frac{2E_{LR}}{\lambda\lambda_z}\left(\Omega_4 + \lambda^2\lambda_z^2\Omega_5 + \lambda^4\lambda_z^4\Omega_6\right),\\
D_\theta &= 0,\\
D_z &= -\lambda_z\Omega_9 - \lambda_z^3\Omega_{10}.
\end{aligned} \tag{25}
$$

We can see that although the applied electric field is purely radial, a nontrivial axial electric displacement component D_z emerges as a consequence of the electromechanical coupling between the axial fiber stretch and the radial electric field. This coupling effect stems from the material anisotropy introduced by the fiber reinforcement, which breaks the axial symmetry of the purely radial field configuration and induces polarization along the fiber direction.

For the axisymmetric deformation and purely radial electric field considered here, the energy function reduces to

$$
\Omega = \Omega\left(\lambda, \lambda_z, E_{LR}\right), \tag{26}
$$

which depends only on the circumferential stretch λ, axial stretch λ_z, and the Lagrangian radial electric field E_{LR}. From Eqs. (23–26), three fundamental differential relations emerge:

$$
D_{LR} = -\frac{\partial\Omega}{\partial E_{LR}}, \quad \tau_{\theta\theta} - \tau_{rr} = \lambda\frac{\partial\Omega}{\partial\lambda}, \quad \tau_{zz} - \tau_{rr} = \lambda_z\frac{\partial\Omega}{\partial\lambda_z}. \tag{27}
$$

These relations are central to the subsequent equilibrium analysis and will be used extensively in deriving the governing equations.

3.2 Equilibrium Equations and Governing Integral Equation

For the axisymmetric deformation under consideration, the equilibrium Eq. (7) reduces to

$$
\frac{\mathrm{d}\tau_{rr}}{\mathrm{d}r} + \frac{1}{r}\left(\tau_{rr} - \tau_{\theta\theta}\right) = 0. \tag{28}
$$

Utilizing the differential relation $(27)_2$ and the transformation (22), Eq. (28) can be rewritten as

$$
\frac{\mathrm{d}\tau_{rr}}{\mathrm{d}\lambda} = \frac{1}{1-\lambda_z\lambda^2}\frac{\partial\Omega}{\partial\lambda}. \tag{29}
$$

Integrating from λ_i to an arbitrary λ and applying the inner boundary condition $\tau_{rr}(r_\mathrm{i}) = -P$, we obtain

$$
\tau_{rr}(\lambda) = \int_{\lambda_\mathrm{i}}^{\lambda} \frac{1}{1-\lambda_z\lambda^2}\frac{\partial\Omega}{\partial\lambda}\mathrm{d}\lambda - P. \tag{30}
$$

Applying the traction-free boundary condition at the outer surface, $\tau_{rr}(r_\mathrm{o}) = 0$, to Eq. (30) yields the fundamental governing equation:

$$
\int_{\lambda_\mathrm{i}}^{\lambda_\mathrm{o}} \frac{1}{1-\lambda_z\lambda^2}\frac{\partial\Omega}{\partial\lambda}\mathrm{d}\lambda = P. \tag{31}
$$

The circumferential and axial stresses follow directly from Eq. (27):

$$
\tau_{\theta\theta} = \tau_{rr} + \lambda\frac{\partial\Omega}{\partial\lambda}, \quad \tau_{zz} = \tau_{rr} + \lambda_z\frac{\partial\Omega}{\partial\lambda_z}. \tag{32}
$$

For tubes with closed ends, the resultant axial force applied at the tube ends is

$$
F = 2\pi\int_{r_\mathrm{i}}^{r_\mathrm{o}} \tau_{zz} r\mathrm{d}r - \pi r_\mathrm{i}^2 P. \tag{33}
$$

Using integration by parts with the equilibrium Eq. (28) and the boundary conditions, this simplifies to [28, 29]

$$
\begin{aligned}
F &= \pi\int_{r_\mathrm{i}}^{r_\mathrm{o}} \left(2\lambda_z\frac{\partial\Omega}{\partial\lambda_z} - \lambda\frac{\partial\Omega}{\partial\lambda}\right) r\mathrm{d}r\\
&= \pi R_\mathrm{i}^2\int_{\lambda_\mathrm{i}}^{\lambda_\mathrm{o}} \lambda\left(2\lambda_z\frac{\partial\Omega}{\partial\lambda_z} - \lambda\frac{\partial\Omega}{\partial\lambda}\right)\frac{1-\lambda_z\lambda_\mathrm{i}^2}{\left(1-\lambda_z\lambda^2\right)^2}\mathrm{d}\lambda,
\end{aligned} \tag{34}
$$

where the relationship (22) has been used.

3.3 Electric Field Distribution and Voltage Constraint

From the Maxwell Eq. $(6)_2$, $\mathrm{div}\mathbf{D} = 0$ reduces to

$$
\frac{1}{r}\frac{\mathrm{d}(rD_r)}{\mathrm{d}r} = 0, \tag{35}
$$

from which we obtain $D_r = K/r$, where K is a constant to be determined. From the constitutive relation $(25)_1$, the radial component of the true electric field is

$$
\begin{aligned}
E_r &= -\frac{\lambda^2\lambda_z^2 D_r}{2}\left(\Omega_4 + \lambda^2\lambda_z^2\Omega_5 + \lambda^4\lambda_z^4\Omega_6\right)^{-1}\\
&= -\frac{\lambda^2\lambda_z^2 K}{2r}\left(\Omega_4 + \lambda^2\lambda_z^2\Omega_5 + \lambda^4\lambda_z^4\Omega_6\right)^{-1}.
\end{aligned} \tag{36}
$$

The constant K can be determined from the applied voltage:

$$
V = \int_{r_\mathrm{i}}^{r_\mathrm{o}} E_r\mathrm{d}r. \tag{37}
$$

This integral equation, together with the geometric relation (21) and Eq. (31), constitutes a complete system for determining the deformation state characterized by the variables λ_i, λ_o, P, V, and λ_z. For given structural geometry and material constants, this system can be solved to obtain the nonlinear electromechanical response of the tube under prescribed loading conditions.

3.4 Thin-Wall Approximation

For thin-walled tubes where $t \to 1$, defining

$$f(\lambda) = \lambda\left(2\lambda_z \frac{\partial \Omega}{\partial \lambda_z} - \lambda \frac{\partial \Omega}{\partial \lambda}\right)\frac{1-\lambda_z\lambda_i^2}{\left(1-\lambda_z\lambda^2\right)^2} \tag{38}$$

and using Taylor expansion with $\bar{\lambda} = (\lambda_i + \lambda_o)/2$ and $\Delta\lambda = \lambda_o - \lambda_i$, the governing Eq. (34) simplifies to

$$F = \pi R_i^2 \left\{ \Delta\lambda f(\bar{\lambda}) + \frac{(\Delta\lambda)^3}{24} f''(\bar{\lambda}) + O[\Delta\lambda]^5 \right\}. \tag{39}$$

We note that the thin-wall expansion procedure adopted here is analogous to that developed by Fu et al. [30] in the purely mechanical context; it provides a computationally efficient semi-analytical solution for membrane-like structures, which is particularly valuable for energy functions with complex forms, where the integral in Eq. (31) cannot be evaluated analytically.

4 Constitutive Models and Loading Methods

4.1 Ideal Dielectric Elastomer

For an ideal dielectric material, the energy function adopts the simple additive form [31]

$$\Omega = W^e\left(I_1, I_2, I_7, I_8\right) - \frac{\varepsilon}{2} I_5 = W^e\left(\lambda, \lambda_z\right) - \frac{\varepsilon}{2}\lambda^2\lambda_z^2 E_{LR}^2, \tag{40}$$

where W^e denotes the purely mechanical strain energy and the term $-\frac{\varepsilon}{2}I_5 = -\frac{\varepsilon}{2}\lambda^2\lambda_z^2 E_{LR}^2$ represents the electrostatic energy, with ε being the permittivity.

For this model, combining Eqs. (36) and (37), the electric field distribution is found to be

$$E_r = \frac{V}{\ln \bar{r}_o}\frac{1}{r}, \quad E_{LR} = \frac{V}{\lambda\lambda_z \ln \bar{r}_o}\frac{1}{r}, \tag{41}$$

where $\bar{r}_o = r_o/r_i$ is the deformed radius ratio.

Introducing dimensionless variables

$$\begin{gathered} \bar{V} = \frac{V}{R_o - R_i}\sqrt{\frac{\varepsilon}{\mu}}, \quad \bar{\tau}_{ij} = \frac{\tau_{ij}}{\mu}, \quad \bar{W}^e = \frac{W^e}{\mu}, \\ \bar{P} = \frac{P}{\mu}, \quad \bar{F} = \frac{F}{\pi(R_o^2 - R_i^2)\mu}, \end{gathered} \tag{42}$$

where μ is the initial shear modulus, the voltage-stretch relation becomes

$$\bar{V} = \frac{t\bar{r}_i \ln \bar{r}_o}{1-t}\sqrt{\frac{2}{1-t^2}\left[g(\lambda_o) + \bar{P}\right]}, \quad \text{with} \quad g(\lambda) = \int_{\lambda_i}^{\lambda} \frac{1}{1-\lambda_z\lambda^2}\frac{\partial \bar{W}^e}{\partial \lambda} d\lambda. \tag{43}$$

Substituting Eq. (40) into (30), the radial stress is obtained as

$$\tau_{rr} = \mu g(\lambda) + \frac{\varepsilon}{2}\left(\frac{V}{\ln \bar{r}_o}\right)^2\left(\frac{1}{r^2} - \frac{1}{r_i^2}\right) - P, \tag{44}$$

where the first term represents the mechanical contribution and the second term arises from the Maxwell stress.

4.2 Ideal Gent Dielectric Model

For materials exhibiting a strain-stiffening effect, the Gent-type energy is employed:

$$W^e = -\frac{\mu J_m}{2}\ln\left(1 - \frac{\lambda^2 + \lambda^{-2}\lambda_z^{-2} + \lambda_z^2 - 3}{J_m}\right) + \frac{\mu}{2}\xi(\lambda_z^2 - 1)^2, \tag{45}$$

where J_m characterizes the limiting chain extensibility and ξ is the fiber reinforcement parameter [32]. Notably, when λ_z is prescribed, ξ does not enter the governing Eq. (31)—it only affects the axial force through Eq. (34). In the limit as $J_m \to \infty$, the Gent model reduces to the so-called neo-Hookean model [31].

Substituting Eq. (45) into the definition (43) and integrating yields

$$\begin{aligned} g(\lambda) = \frac{J_m}{4}\Bigg[&-4\ln\frac{\lambda}{\lambda_i} + \left(1 + \frac{\sqrt{-4+\eta^2}}{2+\eta}\right)\ln\frac{2\lambda^2\lambda_z + \eta - \sqrt{-4+\eta^2}}{2\lambda_i^2\lambda_z + \eta - \sqrt{-4+\eta^2}} \\ &+ \left(1 - \frac{\sqrt{-4+\eta^2}}{2+\eta}\right)\ln\frac{2\lambda^2\lambda_z + \eta + \sqrt{-4+\eta^2}}{2\lambda_i^2\lambda_z + \eta + \sqrt{-4+\eta^2}}\Bigg], \end{aligned} \tag{46}$$

where $\eta = \lambda_z\left(\lambda_z^2 - J_m - 3\right)$. This provides an analytical framework for capturing the nonlinear stiffening behavior characteristic of elastomeric materials at large strains.

4.3 Loading Protocols

In this study, as shown in Fig. 2, we consider two distinct loading protocols for the dielectric elastomer tube subjected to radial voltage V and internal pressure P, each representing different practical constraints and engineering applications:

- **Protocol I: Fixed Ends (Axially Constrained).** The top and bottom ends of the tube are rigidly fixed, preventing any axial deformation. Under the combined action

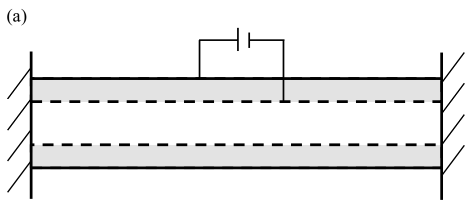

Fig. 2 Schematic diagrams of two loading protocols for dielectric elastomer tubes: **a** Protocol I with fixed ends (axially constrained), where both ends are rigidly clamped; **b** Protocol II with free ends (axially unconstrained), where the ends are free to move in the axial direction. Gray layers represent the dielectric elastomer, and a radial voltage V is applied between the inner and outer electrodes, generating a radially directed electric field through the thickness of the dielectric elastomer

of voltage V and internal pressure P, only the circumferential strain λ changes while the axial stretch λ_z remains constant. This constraint is particularly relevant for applications where the tube is clamped or bonded at both ends.

- **Protocol II: Free Ends (Axially Unconstrained).** The top and bottom ends of the tube are free to move. Under the application of voltage V and internal pressure P, both the circumferential strain λ and the axial strain λ_z change simultaneously. This configuration allows the tube to expand or contract freely in both radial and axial directions. Here, "axially unconstrained" means force-free axial deformation rather than arbitrary rigid-body translation. The latter is excluded by the kinematic assumption $z = \lambda_z Z$.

These two loading protocols lead to fundamentally different deformation responses and stability characteristics. The comparison between these two protocols provides valuable insights for the design and optimization of dielectric elastomer tube-based devices across diverse engineering domains.

5 Numerical Results and Discussion

In this section, we present numerical calculations to illustrate the nonlinear electromechanical response of fiber-reinforced dielectric elastomer tubes under combined radial voltage, internal pressure, and axial loading. All physical quantities are presented in dimensionless form as defined in the previous section. We consider two distinct loading scenarios: axially constrained tubes with prescribed end displacement, and axially free tubes subjected to applied axial force. Unless otherwise stated, calculations are performed with geometric parameter $t = 0.8$, zero internal pressure $\overline{P} = 0$, and Gent parameter $J_m = 97.2$ [33].

5.1 Response of Axially Constrained Tubes

Figure 3 shows the evolution of the inner circumferential stretch λ_i as a function of the applied voltage $\overline{V}$ for axially constrained tubes with different levels of axial pre-stretch $\lambda_z = 1.0, 1.3, 1.8$. For the material model (45), when the axial stretch is held constant, the fiber stiffness parameter ξ does not influence the $\lambda_i - \overline{V}$ relationship, as can be seen from the governing Eq. (31). The results reveal that λ_i increases monotonically with increasing voltage, independent of the magnitude of λ_z. Initially, the response is nearly flat, indicating that small voltages produce minimal circumferential expansion. However, once $\overline{V}$ exceeds a certain threshold, the curves exhibit a sharp upward trend, signifying that the circumferential stretch becomes highly sensitive to voltage variations. At this stage, even a slight increase in voltage can induce substantial radial expansion. Axial stretching causes the tube to contract circumferentially due to incompressibility, resulting in $\lambda_i < 1$ for $\lambda_z > 1$ in the absence of voltage. However, the application of a radial electric field generates Maxwell stresses that drive radial expansion, leading to $\lambda_i > 1$. As observed in Fig. 3, the application of the axial pre-stretch enhances the electromechanical coupling: for a

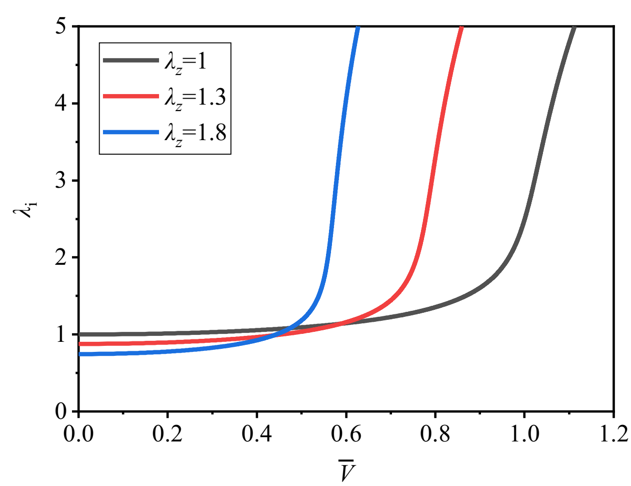

Fig. 3 Inner circumferential stretch λ_i versus applied voltage $\overline{V}$ for axially constrained fiber-reinforced DE tubes with different axial pre-stretches. Parameters: $t = 0.8, \overline{P} = 0, J_m = 97.2, \xi = 0$

given circumferential deformation, a tube subjected to larger λ_z requires a lower driving voltage, thereby reducing the risk of electrical breakdown. This finding suggests a practical design strategy whereby controlled axial pre-stretch can enhance the actuation strain while maintaining safe operating voltages below the dielectric strength of the material.

The fiber stiffness parameter ξ, while not affecting the $\lambda_\mathrm{i} - \overline{V}$ relationship under fixed axial stretch, significantly influences the magnitude of the axial force required to maintain a given deformation state. This is evident from the force equilibrium Eq. (34), where fibers contribute an additional stress component proportional to their stiffness. Figure 4 illustrates the relationship between the axial force $\overline{F}$ and the inner circumferential stretch λ_i for different fiber stiffness parameters $\xi = 0, 0.1, 0.2$ and applied voltages $\overline{V} = 0, 0.2, 0.3, 0.5$. When no voltage is applied, the $\overline{F} - \lambda_\mathrm{i}$ curves are monotonic: under axial tension the tube contracts circumferentially, whereas under axial compression it expands circumferentially. In this purely mechanical regime, the fiber stiffness parameter has negligible influence on the response.

However, when both axial force and electric field are applied simultaneously, electromechanical coupling introduces complex nonmonotonic behavior in the $\overline{F} - \lambda_\mathrm{i}$ relationship. When the axial force is small, mechanical loading dominates the response and increasing force causes the tube to thin down, leading to circumferential contraction. As the thickness decreases, the true electric field in the material increases since the voltage is held constant while the thickness diminishes. At a critical point, the electrostatic Maxwell stress overtakes the mechanical stress as the dominant driving mechanism. Consequently, further increase in axial force counterintuitively causes circumferential expansion due to enhanced voltage-induced deformation. For sufficiently large axial force, strain-stiffening effects in the material prevent further thickness reduction, as captured by the Gent model's limiting stretch. At this stage, the mechanical force regains dominance and circumferential stretch decreases again with increasing force. It is also noteworthy that the influence of the applied voltage is significantly weaker in the compressive regime ($\overline{F} < 0$) than in the tensile regime. This asymmetry can be understood from the incompressibility constraint: under axial compression, the tube wall thickens, so the true electric field $E_r \propto 1/r$ is distributed over a larger radial extent and its magnitude at any given radial position is reduced. Consequently, the Maxwell stress contribution, which scales as E_r^2, becomes relatively small compared with the rapidly growing mechanical restoring stress associated with circumferential expansion. In contrast, under axial tension the wall thins considerably, concentrating the electric field and thereby amplifying the electromechanical coupling. This thickness-mediated mechanism explains why the $\overline{F} - \lambda_\mathrm{i}$ curves in Fig. 4 are nearly insensitive to voltage variations in the compressive branch while exhibiting pronounced voltage dependence in the tensile branch. Comparison of panels (a)–(c) in Fig. 4 reveals an important stabilizing effect of fiber reinforcement: introducing axial fibers suppresses the nonmonotonic snap-through behavior observed in the $\overline{F} - \lambda_\mathrm{i}$ curves. As the fiber stiffness increases, the region of instability becomes less pronounced and the response becomes more stable. This finding suggests that fiber reinforcement can be strategically employed to design DE tubular actuators with stable and predictable actuation characteristics [21, 22].

The role of material constitutive behavior in determining the electromechanical response is further illustrated in Fig. 5, which compares the $\overline{F} - \lambda_\mathrm{i}$ curves obtained using the Gent model (solid lines) and the neo-Hookean model (dashed lines) for different applied voltages. The key distinction between these two models lies in their strain-limiting characteristics. The Gent model incorporates a

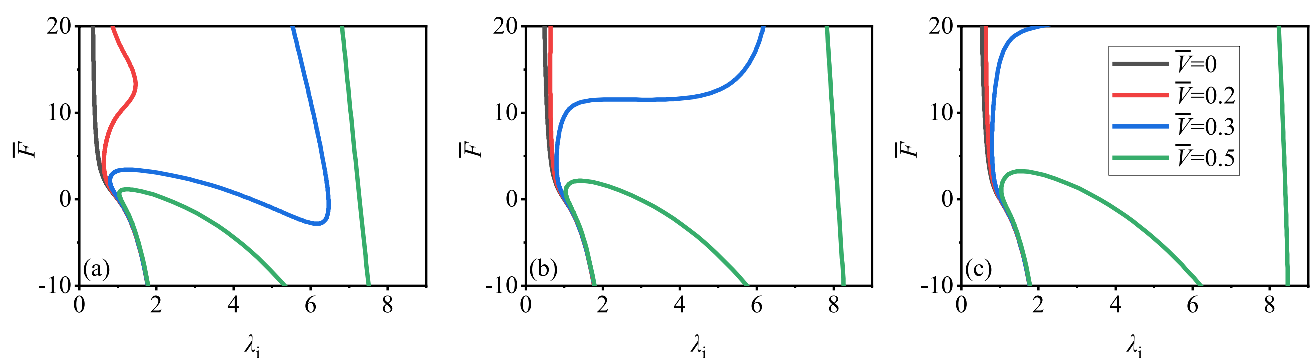

Fig. 4 Axial force $\overline{F}$ versus inner circumferential stretch λ_i for fiber-reinforced DE tubes with different fiber stiffness parameters: **a** $\xi = 0$; **b** $\xi = 0.1$; **c** $\xi = 0.2$. Parameters: $t = 0.8, \overline{P} = 0, J_m = 97.2$

strain-stiffening effect through the parameter J_m, which enforces a finite extensibility limit, whereas the neo-Hookean model permits unbounded deformation. This difference has a profound effect on the tube's response under combined electromechanical loading. For the neo-Hookean material, the thickness continues to decrease indefinitely during the electrically dominated stage, and consequently the mechanical force never regains dominance at large deformations. This renders the neo-Hookean tube susceptible to catastrophic thinning and electrical breakdown at high voltages [34]. In contrast, for the Gent material, the strain-limiting parameter prevents unbounded thickness reduction. Once the deformation approaches the limiting value, the material exhibits dramatic strain-stiffening, which stabilizes the thickness and allows the axial force to reassert mechanical control. This comparison underscores the importance of selecting constitutive models with realistic strain-limiting behavior when predicting the electromechanical response of DE structures [35].

5.2 Response of Axially Free Tubes

We now turn to the case of axially free tubes, where the axial stretch λ_z is not prescribed but instead determined by the force-free condition $\overline{F} = 0$. This configuration is representative of DE tubes used as soft actuators where the ends are unconstrained. Figure 6 presents the voltage-deformation response for axially free fiber-reinforced DE tubes with different fiber stiffness parameters $\xi = 0, 0.5, 1.0$. Both the circumferential stretch λ_i and the axial stretch λ_z are plotted as functions of the applied voltage $\overline{V}$. Under the action of radial voltage, the axially free tube expands both circumferentially and axially, as evidenced by $\lambda_i > 1$ and $\lambda_z > 1$. A striking feature of the response curves is their characteristic

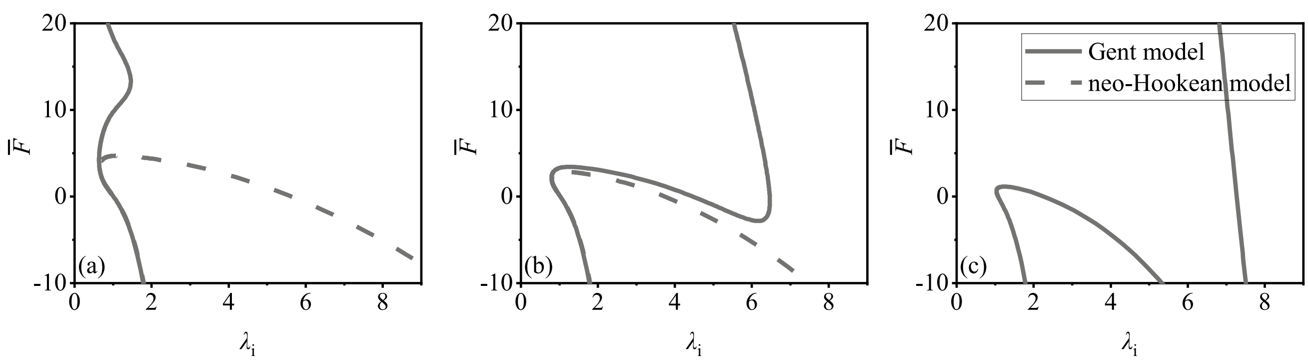

Fig. 5 Comparison of axial force $\overline{F}$ versus inner circumferential stretch λ_i for Gent model (solid lines) and neo-Hookean model (dashed lines) with different applied voltages: **a** $\overline{V} = 0.2$; **b** $\overline{V} = 0.3$; **c** $\overline{V} = 0.4$ (In this case, the solid line and the dashed line coincide, so the dashed line is not displayed). Parameters: $t = 0.8, \overline{P} = 0, J_m = 97.2, \xi = 0$

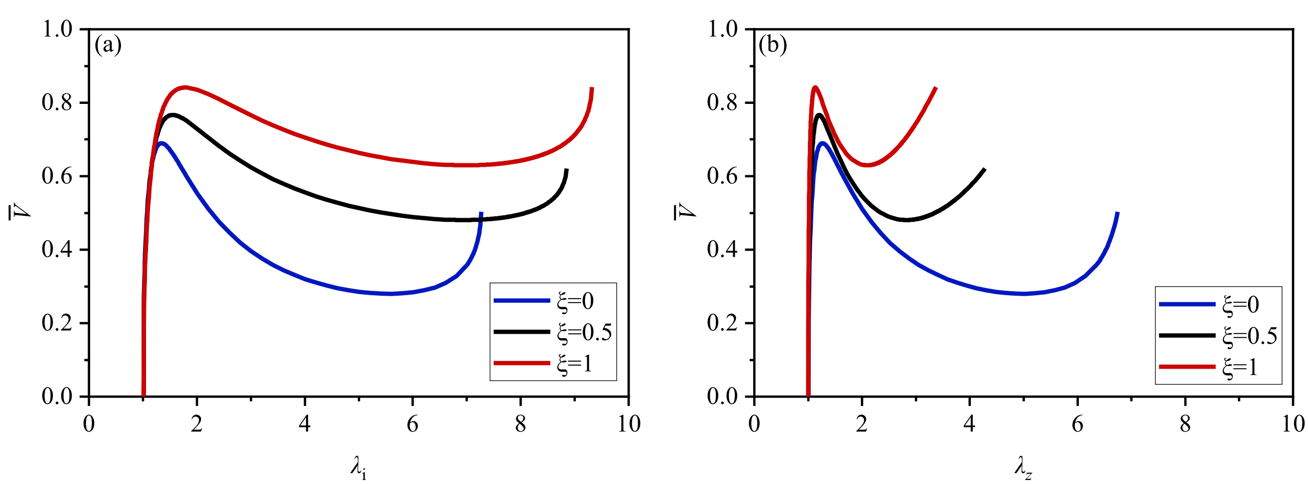

Fig. 6 Effect of fiber stiffness ξ on the nonlinear response of axially free fiber-reinforced DE tubes: **a** Applied voltage $\overline{V}$ versus inner circumferential stretch λ_i; **b** Applied voltage $\overline{V}$ versus axial stretch λ_z. Parameters: $t = 0.8, \overline{P} = 0, \overline{F} = 0, J_m = 97.2$

N-shaped nonmonotonic behavior, which is fundamentally different from the monotonic response observed in axially constrained tubes (Fig. 3). This nonmonotonicity indicates the presence of a snap-through instability [20].

Initially, when the voltage is small, the tube deforms gradually and the response is stable. However, as the voltage reaches a critical threshold, the electrostatic attraction between the electrodes overcomes the elastic restoring force, triggering a sudden jump in deformation. During this instability, the tube undergoes rapid radial expansion accompanied by dramatic thickness reduction, which significantly increases the risk of electrical breakdown. For the Gent material, the strain-limiting effect arrests the runaway deformation when the stretch approaches its maximum allowable value. As the voltage continues to increase beyond the snap-through point, the deformation growth rate slows down due to strain-stiffening. An important observation from Fig. 6 is that increasing the fiber stiffness raises the critical voltage threshold for snap-through instability. This stabilizing effect arises because stiffer axial fibers resist the voltage-induced elongation, thereby delaying the onset of instability. Consequently, fiber reinforcement provides an effective strategy to enhance the electromechanical stability of DE tubular actuators and expand their safe operating voltage range.

5.3 Response of Thin-Walled Tubes

For thin-walled tubes with $t \to 1$, the through-thickness variation of stress and electric field becomes negligible, and simplified analytical expressions can be derived based on membrane theory (39). Figure 7 validates the accuracy of the thin-wall approximations by comparing them with the exact analytical solution. The results demonstrate that for tubes with $t = 0.9$, the first-order approximation yields a maximum error of approximately 5.7%, while the second-order approximation reduces the error to less than 0.6%. This excellent agreement validates the membrane approximation and confirms its utility for rapid parametric studies involving thin-walled fiber-reinforced DE tubes. It is worth noting that the approximation becomes increasingly accurate as $t \to 1$. For thicker tubes with $t < 0.8$, the through-thickness variation of fields becomes significant, and the full analytical solution or numerical integration is required for accurate predictions.

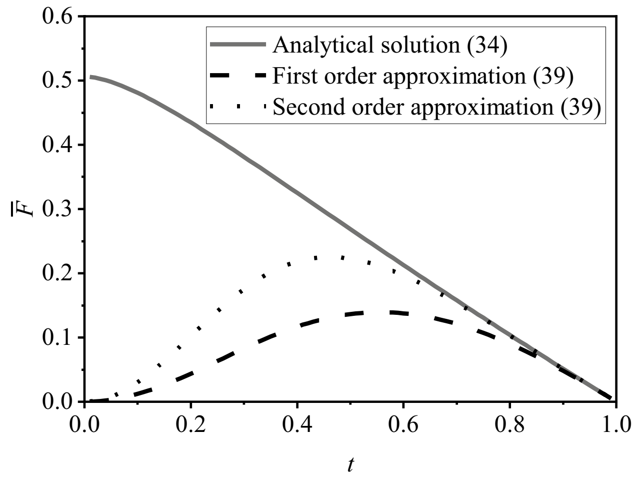

Fig. 7 Comparison of the exact analytical solution for axial force $\overline{F}$ with first-order and second-order thin-wall approximations as functions of the thickness ratio t. Parameters: $\lambda_z = 1.2, \lambda_i = 1.2, \overline{P} = 0, \xi = 0, J_m = 97.2$

6 Conclusions

This paper has developed a theoretical framework for analyzing the finite electromechanical deformation of axially fiber-reinforced dielectric elastomer tubes subject to combined radial electric field, internal pressure, and axial loading. Based on the nonlinear theory of electroelasticity for transversely isotropic materials, we have derived analytical solutions for the deformation, stress distribution, and electric field in thick-walled cylindrical tubes with fibers aligned along the axial direction.

The formulation introduces additional invariants associated with the fiber direction into the electroelastic energy function, accommodating arbitrary forms of anisotropic strain-energy functions while accounting for full electromechanical coupling. Analytical solutions have been obtained for thick-walled tubes under radial voltage, internal pressure, and prescribed axial stretch or axial force. Closed-form expressions for the stress components and electric field distribution have been derived for a specific class of ideal fiber-reinforced dielectric materials. For thin-walled tubes, first-order and second-order membrane approximations provide highly accurate predictions with minimal computational cost, validated against exact solutions with sub-percent errors for slender geometries.

The interplay between voltage-induced radial expansion and mechanically driven axial deformation gives rise to complex nonlinear and nonmonotonic response characteristics. In axially constrained tubes, electromechanical coupling leads to multistage competitive behavior between mechanical and electrical effects, resulting in N-shaped force–deformation curves under combined tension and voltage. Axial fiber reinforcement fundamentally alters the electromechanical stability of DE tubes by resisting voltage-induced elongation and suppressing snap-through instabilities, thereby expanding the safe operating voltage range. Axial pre-stretch serves as an effective mechanism to enhance actuation performance, as imposing a prescribed axial elongation significantly reduces the voltage required for a given circumferential expansion, lowering the risk of electrical breakdown. Material strain-limiting characteristics play a critical role in determining post-instability behavior, with constitutive models incorporating finite extensibility preventing catastrophic thinning, whereas models without limiting stretch predict unbounded instability-driven expansion leading to electrical failure.

From a design perspective, the results suggest that by selecting the fiber stiffness parameter appropriately, designers can tune the balance between axial stiffness and radial compliance, enabling directional actuation tailored to specific application requirements. From a practical standpoint, the present results offer several quantitative design guidelines for fiber-reinforced dielectric elastomer tubular actuators.

First, for applications requiring large radial actuation stroke, such as peristaltic pumps or soft grippers, imposing a moderate axial pre-stretch can substantially reduce the driving voltage needed to achieve a target circumferential expansion, thereby lowering the risk of electrical breakdown and extending device lifetime.

Second, for actuators operating under combined pressure and voltage, the fiber stiffness parameter ξ can be tuned to suppress snap-through instabilities: our results indicate that even modest fiber reinforcement markedly stabilizes the force–deformation response, making the actuation characteristic more predictable and controllable.

Third, the choice of constitutive model, in particular the strain-limiting parameter J_m, has direct implications for the safe operating envelope: materials with finite extensibility provide an intrinsic safeguard against catastrophic thinning and electrical failure, suggesting that elastomers with pronounced strain-stiffening behavior are preferable for high-voltage applications.

These guidelines are expected to be useful for the design of next-generation soft robotic actuators, artificial muscles, and adaptive structures based on fiber-reinforced dielectric elastomer tubes.

Acknowledgements This work was supported by the National Natural Science Foundation of China (Nos. 12402193, 12202171, and 12192210) and the Natural Science Foundation of Zhejiang Province (Nos. LR26A020003 and LMS25A020005). The work of MD was supported by a Qiushi Guest Professor appointment (Seagull Program) at Zhejiang University.

Funding National Natural Science Foundation of China, 12402193, Yipin Su, 12202171, Guozhan Xia, 12192210, Weiqiu Chen, Natural Science Foundation of Zhejiang Province, LR26A020003, Yipin Su, LMS25A020005, Congshan Liu, Qiushi Guest Professor appointment (Seagull Program) at Zhejiang University.

Declarations

Conflict of interest The authors declare that there are no conflicts of interest regarding the publication of this paper.

References

1. Pelrine R, Kornbluh R, Pei Q, Joseph J. High-speed electrically actuated elastomers with strain greater than 100%. Science. 2000;287(5454):836–9.
2. Cao X, Zhang M, Zhang Z, Xu Y, Xiao Y, Li T. Review of soft linear actuator and the design of a dielectric elastomer linear actuator. Acta Mech Solida Sin. 2019;32(5):566–79.
3. Gu GY, Zhu J, Zhu LM, Zhu X. A survey on dielectric elastomer actuators for soft robots. Bioinspir Biomim. 2017;12(1):011003.
4. Guo Y, Liu L, Liu Y, Leng J. Review of dielectric elastomer actuators and their applications in soft robots. Adv Intell Syst. 2021;3(10):2000282.
5. Youn JH, Jeong SM, Hwang G, Kim H, Hyeon K, Park J, et al. Dielectric elastomer actuator for soft robotics applications and challenges. Appl Sci. 2020;10(2):640.
6. Zhao M, Jiang W, Wang Q, Liang Y, Fan H, Tian X. Total internal reflection (TIR) behavior of heterogeneous interface shear waves in layered soft structure. Acta Mech Solida Sin. 2024;37(5):662–72.
7. Mannsfeld SCB, Tee BCK, Stoltenberg RM, Chen CVHH, Barman S, Muir BVO, et al. Highly sensitive flexible pressure sensors with microstructured rubber dielectric layers. Nat Mater. 2010;9:859–64.
8. Duduta M, Hajiesmaili E, Zhao H, Wood RJ, Clarke DR. Realizing the potential of dielectric elastomer artificial muscles. Proc Natl Acad Sci USA. 2019;116(7):2476–81.
9. An L, Wang F, Cheng S, Lu T, Wang TJ. Experimental investigation of the electromechanical phase transition in a dielectric elastomer tube. Smart Mater Struct. 2015;24(3):035006.
10. Cameron CG, Szabo JP, Johnstone S, Massey J, Leidner J. Linear actuation in coextruded dielectric elastomer tubes. Sens Actuators A Phys. 2008;147(1):286–91.
11. Zhu J, Stoyanov H, Kofod G, Suo Z. Large deformation and electromechanical instability of a dielectric elastomer tube actuator. J Appl Phys. 2010;108(7):074113.
12. Su Y. Voltage-controlled instability transitions and competitions in a finitely deformed dielectric elastomer tube. Int J Eng Sci. 2020;157:103380.
13. Dorfmann L, Ogden RW. Nonlinear Theory of Electroelastic and Magnetoelastic Interactions. New York: Springer; 2014.
14. Su Y, Wu B, Chen W, Destrade M. Finite bending and pattern evolution of the associated instability for a dielectric elastomer slab. Int J Solids Struct. 2019;158:191–209.
15. Bahreman M, Arora N, Darijani H, Rudykh S. Structural and material electro-mechanical instabilities in microstructured dielectric elastomer plates. Eur J Mech A Solids. 2022;94:104534.
16. Zhu F, Wu B, Destrade M, Wang H, Bao R, Chen W. Voltage-controlled non-axisymmetric vibrations of soft electro-active tubes with strain-stiffening effect. Int J Solids Struct. 2024;290:112671.

17. Sharma AK, Kosta M, Shmuel G, Amir O. Gradient-based topology optimization of soft dielectrics as tunable phononic crystals. Compos Struct. 2022;280:114846.
18. Zhang Z, Li J, Liu Y, Xie YX. Nonlinear oscillations of a one-dimensional dielectric elastomer generator system. Extreme Mech Lett. 2022;53:101718.
19. Zhao X, Suo Z. Method to analyze electromechanical stability of dielectric elastomers. Appl Phys Lett. 2007;91(6):061921.
20. Zhao X, Hong W, Suo Z. Electromechanical hysteresis and coexistent states in dielectric elastomers. Phys Rev B. 2007;76(13):134113.
21. Holzer S, Konstantinidi S, Koenigsdorff M, Martinez T, Civet Y, Gerlach G, et al. Fiber-reinforced equibiaxial dielectric elastomer actuator for out-of-plane displacement. Materials. 2024;17(15):3672.
22. Xiao R, Gou X, Chen W. Suppression of electromechanical instability in fiber-reinforced dielectric elastomers. AIP Adv. 2016;6(3):035221.
23. Bustamante R. Transversely isotropic non-linear electro-active elastomers. Acta Mech. 2009;206(3):237–59.
24. Goulbourne NC. A mathematical model for cylindrical, fiber reinforced electro-pneumatic actuators. Int J Solids Struct. 2009;46(5):1043–52.
25. He L, Lou J, Du J, Wu H. Voltage-induced torsion of a fiber-reinforced tubular dielectric elastomer actuator. Compos Sci Technol. 2017;140:106–15.
26. Liu L, Yong H. Bifurcation and post-bifurcation behaviors of fiber-reinforced dielectric elastomer tube actuator under electromechanical loadings. Thin-Walled Struct. 2026;207:114599.
27. Dorfmann L, Ogden RW. Instabilities of an electroelastic plate. Int J Eng Sci. 2014;77:79–101.
28. Melnikov A, Ogden RW. Finite deformations of an electroelastic circular cylindrical tube. Z Angew Math Phys. 2016;67(6):140.
29. Haughton DM, Ogden RW. Bifurcation of inflated circular cylinders of elastic material under axial loading—II. exact theory for thick-walled tubes. J Mech Phys Solids. 1979;27(5–6):489–512.
30. Fu YB, Liu JL, Francisco GS. Localized bulging in an inflated cylindrical tube of arbitrary thickness—the effect of bending stiffness. J Mech Phys Solids. 2016;90:234–50.
31. Su Y, Broderick HC, Chen W, Destrade M. Wrinkles in soft dielectric plates. J Mech Phys Solids. 2018;119:298–318.
32. Zeng C, Gao X. Stability of an anisotropic dielectric elastomer plate. Int J Non-Linear Mech. 2020;124:103510.
33. Dorfmann L, Ogden RW. Nonlinear response of an electroelastic spherical shell. Int J Eng Sci. 2014;85:163–74.
34. Zurlo G, Destrade M, DeTommasi D, Puglisi G. Catastrophic thinning of dielectric elastomers. Phys Rev Lett. 2017;118(7):078001.
35. Huang W, Chen K, Ma P, Kang G. A visco-hyperelastic constitutive model for temperature-dependent cyclic deformation of dielectric elastomer. Acta Mech Solida Sin. 2024;37(5):736–49.